THE JOURNAL OF PHYSICAL CHEMISTRY LETTERS
A JOURNAL OF THE AMERICAN CHEMICAL SOCIETY

pubs.acs.org/JPCL

Letter

Exceptional Spatial Variation of Charge Injection Energies on Plasmonic Surfaces

Xiaohe Lei, Annabelle Canestraight, and Vojtech Vlcek*

Cite This: *J. Phys. Chem. Lett.* 2023, 14, 8470−8476

Read Online

ACCESS | Metrics & More | Article Recommendations | Supporting Information

ABSTRACT: Charge injection into a molecule on a metallic interface is a key step in many photoactivated reactions. We employ the many-body perturbation theory and compute the hole and electron injection energies for CO_2 molecule on an Au nanoparticle with ∼3,000 electrons and compare it to results for idealized infinite surfaces. We demonstrate a surprisingly large variation of the injection energy barrier depending on the precise molecular position on the surface. Multiple "hot spots," characterized by low energy barriers, arise due to the competition between the plasmonic coupling and the degree of hybridization between the molecule and the substrate. The charge injection barrier to the adsorbate on the nanoparticle surface decreases from the facet edge to the facet center. This finding contrasts with the typical picture in which the electric field enhancement on the nanoparticle edges is considered the most critical factor.

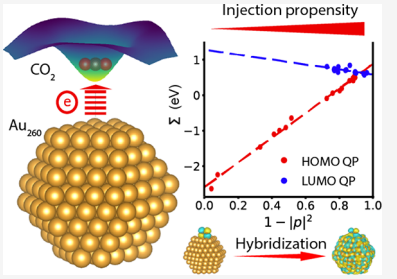

Plasmon-driven interactions on metallic nanostructures are well-known for improving the sensitivity of the optical probes[1] and enabling light-driven reactions.[2−16] The incident electromagnetic radiation induces localized surface plasmon resonance (LSPR) on the subwavelength metal surface, which leads to increased light absorption and scattering.[8,13,16,17] The LSPR coupling to the adsorbate can trigger chemical reactions that are hard to achieve by thermal excitation (e.g., water splitting[12]) and lead to selective reaction pathways (e.g., selective products formation in CO_2 reduction[9,10,14,16]). The interfacial energy transfer following the LSPR decay is critical to understanding such plasmon-mediated mechanism of chemical transformations.[3] The LSPR dephasing is driven by multiple possible scattering channels, including a nonradiative pathway generating "hot" charge carriers, i.e., highly excited and out-of-equilibrium holes and electrons.[2,7,18,19] The efficiency of the interfacial energy transfer via charge carrier injection is affected by multiple factors such as the incident light wavelength; the composition, size, and shape of the nanostructure; the local electric field; and the availability of the adsorbate state.[3,6,11,15,20] The local electric field enhancement by LSPR is known to be an important factor in the design of plasmonic photocatalysts for small molecule activation. The LSPR strength varies spatially across the plasmonic surface. The field at the plasmonic nanostructure junction, or the edge, is typically more enhanced compared to other areas and hence it is determined to be the chemical "hot spot", where the plasmonically driven transformations may preferentially occur.[5,11,14] However, the effective energy barrier for charge injection is derived from the energy level of the adsorbate states. While critical, this aspect of plasmonic transformation hot spots has not been sufficiently studied. In practice, it requires a detailed microscopic description of the coupling between the excited state of the plasmonic substrate and the adsorbate at any given location on the surface. A computational investigation is well-positioned to address this question, where the orbital energies are found by considering the complex many-body interactions between the subsystems. Density functional theory (DFT) is used most frequently, analyzing the charge density distribution[21] and energetics[22−26] in interfacial systems. These calculations are affordable for systems of thousands of electrons.[27] However, DFT eigenvalues do not (even in principle) correspond to the quasi-particle energies, except the system's highest occupied state.[28] In practice, much-improved estimates of individual electronic states are obtained with approximate DFT functionals that minimize self-interaction errors, e.g., with optimally tuned range-separated functionals in which the asymptotic form of the nonlocal exchange is attenuated, similar to the application of static screening.[25,26,29−35] Yet, these methods are typically limited to the mean-field description, and they neglect nonlocality and potentially significant anisotropy of the dynamical screening. Further, the extension to new excited state signatures due to strong couplings between the single electron or hole excitation and the dynamical fluctuations necessitates to go beyond DFT.[36,37]

We overcome these limitations by employing many-body perturbation theory (MBPT) in the *GW* approximation

Received: August 9, 2023
Accepted: September 12, 2023
Published: September 18, 2023

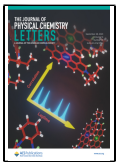

(GWA) to solve for the energies of individual single excited electrons and holes "dressed" by their interactions with the environment (i.e., quasiparticles − QPs).[28,38] In GWA, the QP propagator, represented by the Green's function (G), is renormalized by nonlocal correlation effects stemming from charge density fluctuations on the molecule and the substrate. The screened Coulomb interaction (W) contains the nonlocal interactions with the underlying plasmonic "reservoir" which affects molecular QP energies.[28,38,39] In this work, we use the G_0W_0 approximation, where both Green's function and the screened Coulomb interaction are constructed using the DFT eigenstates. Rather than self-consistently solving for the Green's function of the true QP states, a one shot correction to the KS Hamiltonian is applied. This method has been shown to improve the predictions of both experimental band-gaps and molecular ionization potentials, making it a strong theoretical tool for treating a molecule-metal interface.[40−44] However, the scaling of this algorithm has prevented its use in studying realistic systems.[45,46] To remedy this, we use the stochastic *GW* formalism which reduces the computational scaling and allows us to handle systems with thousands of electrons, enabling this study.[40,47] We investigate CO_2 on gold, a prototypical surface−adsorbate system where the small molecule acts as a probe of the local coupling of an excited molecular state to the metal substrate. Large slabs and a full nanoparticle (NP) with thousands electrons are used as the gold substrate. We complement the light-enhancement-driven reactivity picture by identifying the "hot spots" with the minimal energy barrier for (vertical) hot charge injection to the adsorbate. We study the molecular QP energies corresponding to the lowest hole for electron injection energy onto the adsorbate across varied positions on Au surfaces. The electron injection process corresponds to the vertical excitation in the proposed mechanism of the fist step in CO_2 reduction, forming the transient negative ion intermediate.[16,21,48]

Our results demonstrate a remarkable variation of the molecular QP energies depending on the exact position on the surface (here corresponding to various facets of an NP). Accounting for nonlocal many-body interactions leads to changes on the order of up to several hundreds of meV and significantly affects the predicted energy barrier for charge injection, i.e., the distance from the substrate Fermi level. Our results indicate that the plasmonically driven chemical "hot spots" are affected by a nontrivial interplay between the adsorbate's sensitivity to the underlying plasmonic field and the adsorbate orbital hybridization with the delocalized surface states. In contrast to the previous models which study solely the local field enhancement,[11,14] we find that the charge injection barrier *increases* as the molecule approaches the nanostructure edges, which are known to exhibit strong plasmon dephasing and a relative abundance of free charges.

We study the molecule in various positions on Au (111) and (100) surfaces of an infinite slab (generated by 2D periodic boundary conditions) and an Au_{260} NP. The physisorbed CO_2 geometry is optimized using DFT applied to the molecule on a 3-layer Au surface using QuantumEspresso.[49] For selected geometries, we repeated the relaxation with both a thicker gold slab and a wider gold slab to verify that the molecular geometry is insensitive to the increased slab thickness or decreased molecular coverage on the surface (with <0.1% the bond-lengths and angles variation). The geometry optimization is performed on all types of adsorption sites. For (111): fcc hollow site (f), hcp hollow site (h), atomic site (a) and bridge site (b); for (100): hollow site (h), atomic site (a), and bridge site (b). The simulation system name is labeled as the facet index followed by the site initial, e.g., $(111)_f$ for the CO_2 adsorbed at the fcc hollow site on the Au (111) surface. The optimized surface separation is 3.44 Å on (111) and 3.24 Å on (100), with variations across different sites being <5%. The variation of the total energy is minimal (<0.0005% between the minimum of $(111)_f$ and its counterpart $(100)_h$). We use the optimized molecular geometry and molecule−surface separation in relaxed $(111)_f$ and $(100)_h$ for the corresponding lattice surfaces to make a consistent comparison among the computational results. In addition, we have investigated a relaxed structure of CO_2 on the Au (111)/(100) interface ridge. Further details about the structural optimization are in the Supporting Information (SI).

While the molecular geometry is determined primarily by the near-surface Au atoms, the electronic structure of the composite system converges more slowly with the number of gold layers. The fully converged single-particle energies are obtained for slabs with 9 and 13 layers for the (111) and (100) surfaces. These are comparable in dimension to a truncated octahedron Au_{260} NP with (111) and (100) facets (Figure S3), which is a thermodynamically stable form of a gold NP.[17] The molecular geometry and separation are taken from the optimized structure outlined above.

To define the electronic states associated with the adsorbate, we first construct a set of localized molecular states $\{\varphi\}$ constructed as a linear combination of unitary-transformed maximally localized states obtained with the Pipek−Mezey Wannier approach.[50] The $\{\varphi\}$ states span the molecular subspace and conceptually correspond to the states in an isolated molecule in the gas phase.[51,52] We use this step to identify the canonical mean-field states, $\{\phi\}$ (i.e., the delocalized state computed by DFT for the entire molecule−surface system) that have primarily molecular character. We rank the states $\{\phi\}$ according to their projection values $|p_j|^2 = |\langle\varphi_j|\phi\rangle|^2$ where φ_j is a particular molecular state. The $|p|^2$ values for the frontier molecular orbitals (FMOs) are <0.95 due to hybridization, while the bottom valence states exhibit $|p|^2$ very close to unity. Upon adsorption, the interaction with the substrate lifts the degeneracy of the highest occupied state (HOMO). The canonical states with the largest fraction of localized HOMO orbital is considered to be representative of the HOMO state on the surface. For the LUMO, we inspect only the bound states. These have $|p|^2$ values of ≈0.3 at most and thus show more pronounced hybridization with the substrate.

We calculate the QP energies of injected holes and electrons for these most molecule-like canonical orbitals. Employing the G_0W_0 approximation, the QP energy is found through the fixed point equation,

$$\epsilon_{QP} = \epsilon_{KS} + \langle\phi|\hat{\Sigma}_P(\omega = \epsilon_{QP}) + \hat{\Sigma}_X - \hat{v}_{xc}|\phi\rangle \quad (1)$$

where ϵ_{KS} is the DFT starting point eigenvalue, $\hat{v}_{xc}$ is the exchange-correlation potential (approximated by a semilocal DFT functional) and $\hat{\Sigma}_X$ is the nonlocal exchange self-energy and $\hat{\Sigma}_P$ is the dynamical self-energy that accounts for the induced density−density interactions, i.e., it includes the plasmonic response of the substrate.

We first investigated the charge injection to CO_2 adsorbed on infinite Au (111) and (100) surfaces. The QP energy of FMOs varies only by 0.4 eV between the two surfaces. The

https://doi.org/10.1021/acs.jpclett.3c02223
J. Phys. Chem. Lett. 2023, 14, 8470−8476

HOMO QP energy is −12.6 eV on average; this agrees well with the experimental result estimating the center of HOMO state near −12.5 eV.[53] The LUMO is unbound in the gas phase, and its average value on an infinite surface is −1.10 eV. The LUMO "stabilization" (negative energy shift making the orbital bound) due to the surface interaction thus, in principle, enables the CO $_2^-$ intermediate formation important in CO_2 reduction. MBPT is known to correct the DFT results by large shifts,[43,44,54−56] this is also the case here: For the HOMO, the G_0W_0 correction reduces the energy by 3.34 and 3.64 eV in $(111)_f^{inf}$ and $(100)_h^{inf}$. For the LUMO, the QP energy is, on average, 0.38 eV lower than the KS eigenvalue. As a result, we can clearly see that MBPT leads to a significant fundamental band gap opening compared to the DFT results by 35% in $(111)_f^{inf}$ and 40% in $(100)_h^{inf}$ (i.e., 2.86 and 3.35 eV).

We now investigate the charge injection onto the molecule on the Au_{260} NP. The NP exhibits metallic behavior and supports surface plasmon resonance.[17] Since it contains a similar number of Au atoms as the 2D infinite slab, the observed change in the nonlocal correlations should be influenced primarily by the NP shape. There are 8 layers for the Au (111) facet and 9 layers for the Au (100) facet in the NP. Yet, the molecular QP energies on the NP are significantly different from those on an infinite substrate, demonstrating the profound effects of nanoscale surface structure. On average, the QP energies on the NP are higher by 3.11 eV for the hole and 0.70 eV for the electron injection than that of the infinite surface result. The electron injection barrier from the substrate to the CO_2 $E_{QP}^{FMO}-E_f$ is shown to be higher than the simple difference $E_{KS}^{FMO}-E_f$ predicted by DFT. DFT underestimates the energy barrier for electron injection by 20% and that for hole injection by 10%.

These average results, however, smear out the local variation of the barriers. The most surprising discovery is that the QP energy varies significantly depending on the specific position of the molecule on the surface. As shown in Figure 1 (Top panel), for each type of surface site (namely, on (111) facet: f, h, b, a; on (100) facet: h, b, a), we studied at least one facet center position and one facet edge position.

The difference between the center and the edge positions for the LUMO QP energy are as large as 380 meV. Such a difference corresponds to a 1.5kT energetic difference at 298 K. Considering the nonequilibrium process involving highly excited "hot" electron injection (and corresponding Boltzmann factors), this implies the injected electron on the NP facet center is about four-fold "hotter" than it on the NP facet edge. The variation is even more pronounced for HOMO (i.e., and the corresponding hole injection barrier) which varies as much as 3.41 eV (Figure 1). These MBPT results are in striking contrast to mean-field calculations, which show 700% smaller position dependence(for comparison, a heat map obtained with the mean-field result is in Figure S5 and demonstrates a significantly decreased variation of the injection energies). The discrepancy is due to the substrate-induced renormalization, which is missing from the approximate (semilocal) exchange-correlation functional.[23,44,57,58] Our analysis shows that the hole injection is most probable in the center of the (111) facet, with the QP energy level of 2.90 ± 0.08 eV below the Fermi level. The electron injection is also most probable at the center of (111), but we also identified $(100)_{a3}$ edge position to host similarly low QP LUMO energy, with a QP energy of 4.76 ± 0.07 eV above the Fermi level. The overall injection energy variation is clearly related to the surface position.

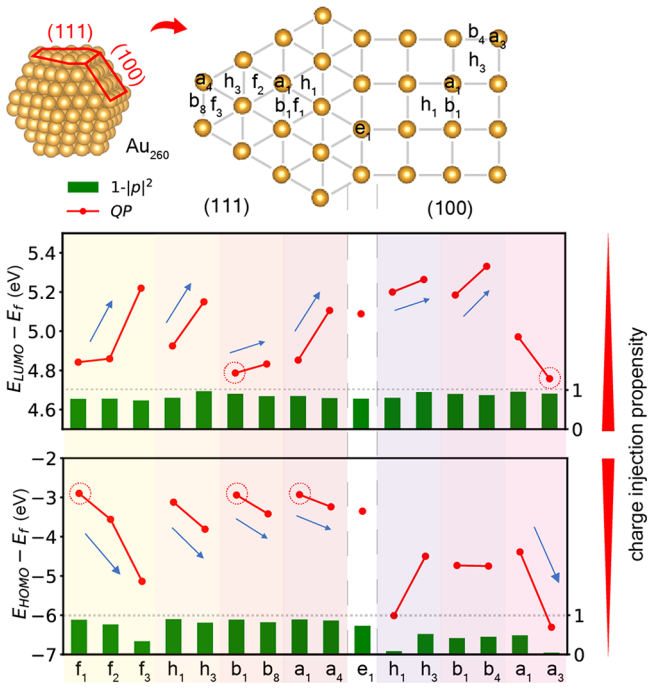

Figure 1. Au_{260} NP consists of 8 hexagon (111) facets and 6 square (100) facets. The surface site map of the NP is displayed on its right. Four types of adsorption sites on the (111) facet are fcc hollow (f), hcp hollow (h), atomic (a), and bridge (b). Three types of adsorption sites on (100) are hollow (h), atomic (a), and bridge (b). The positions are numbered from small to large, corresponding from the facet center position to the edge position. Labels for the symmetrical positions are not repeated. The case CO_2 is put atop the ridge Au atom is labeled as e1. In the QP energy panels, the difference between the QP energy and the Fermi level (red dots) is plotted together with the degree of hybridization of $1 - |p|^2$ values (green bars) for the selected hybridized FMO. Blue arrows indicate the QP energy trend further from the Fermi level when the molecular position approaches the NP facet edge. The data points corresponding to the lowest charge injection barriers are red-circled. the most favored sites for the electron injection are $(111)_{b1}$ and $(100)_{a3}$, with a charge injection barrier at 4.76 ± 0.07 eV; the most favored sites for the hole injection are $(111)_{f1}$, $(111)_{b1}$ and $(111)_{a1}$, with the charge injection barrier at 2.90 ± 0.08 eV.

As the interpolated color map shows (Figure 2), on the NP (111) facet, both the electron and hole injection propensities decrease from the center to the edge. On the NP (100) facet, the center is no longer shown to be the most probable region for charge injection. The corner position is most favorable for the electron injection. As for the hole injection, the side location has the highest charge injection propensity.

The spatial patterns of the charge injection barrier shown in Figure 2(a) depend on multiple factors; here, the degree of hybridization with the surface should play a significant role, as it affects the interaction with the surface states. We will now study the effect of orbital hybridization in greater detail by considering the molecular and substrate self-energy contributions separately. The QP energy shift evaluated for a given canonical state is decomposed into individual contributions based on the projection on the molecular and surface subspaces. For the analysis, we again employed a set of localized states and the values of $|p_j|^2$ defined above. The "molecular contribution" to a particular state: is $|p|^2 = \sum_j |p_j|^2$, while the remainder $(1 - |p|^2)$ is the surface contribution. For HOMO, the summation goes over all localized molecule-like

https://doi.org/10.1021/acs.jpclett.3c02223
J. Phys. Chem. Lett. 2023, 14, 8470−8476

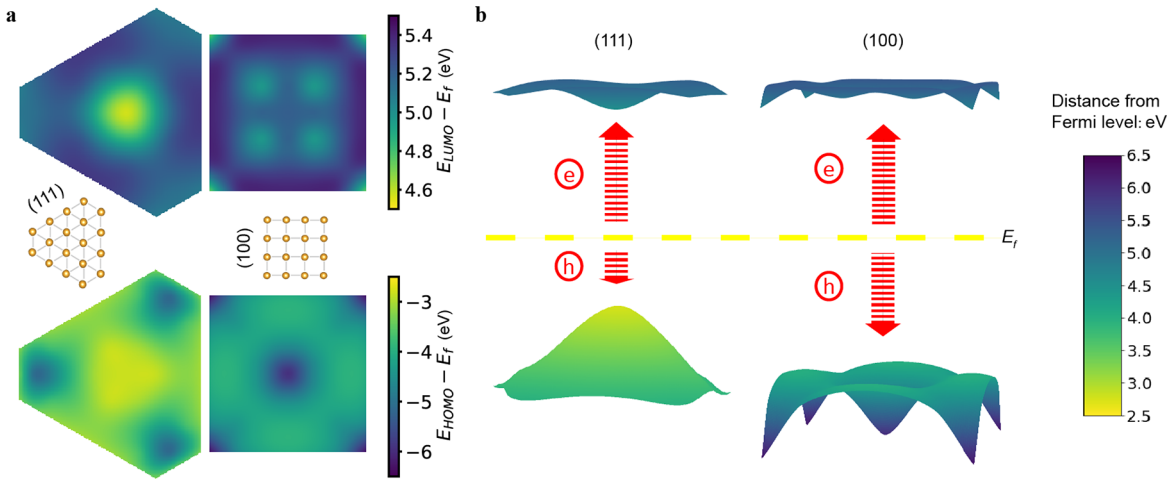

Figure 2. (a) Interpolated heat map of $E_{FMO} - E_f$ on the (111) and (100) facets. The yellow end indicates a smaller injection barrier. (b) Interpolated surface plot of $E_{FMO} - E_f$ on the (111) and (100) facets intuitively displaying exceptional spatial variation of the charge injection energies. A yellow dashed line shows the Fermi level E_f = 5.42 eV. On the (111) facet, the center region is indicated to be the most favored location for both quasi-electron and quasi-hole injections. On (100) facet, the facet corner is indicated to be the most favored site for electron injection; the facet side location is indicated to be the most favored location for hole injection.

occupied states $\{\varphi_j\}$; $j \leq$ HOMO. Below, we will discuss the self-energy dependence on $|p_{\mathrm{HOMO}}|^2$ that exhibits the same behavior, illustrating that the exact definition of the molecular subspace is less critical. For the LUMO state, we restrict the projection only to a single lowest unoccupied state (j = LUMO), as we could not consistently identify another molecular state that would accept an extra electron. This simplistic approach shows that hybridization is a major factor: the spatial pattern of $1 - |p|^2$ values (Figure S5) is remarkably close to the maps shown in Figure 2.

For each FMO, we take the respective magnitudes of its projection onto the molecular and surface subspaces to account for their contributions to the self-energy, as

$$\Sigma = |p|^2\Sigma_{\mathrm{mol}} + (1 - |p|^2)\Sigma_{\mathrm{sub}} \tag{2}$$

This simple relationship that assumes that the molecular and surface subspaces are clearly separated (i.e., disregarding the off-diagonal contributions) corresponds well with our numerical data for Σ as a function of $|p|^2$. The fitted parameters Σ_{mol} and Σ_{sub} are given in the SI. We see in Figure 3 that the injection propensity varies linearly with the degree of hybridization, with a slope of $\Sigma_{\mathrm{sub}} - \Sigma_{\mathrm{mol}}$. Note that the dependence changes when we consider projection on HOMO ($|p_{\mathrm{HOMO}}|^2$) or the entire molecular subspace ($|p|^2$) as illustrated in Figure 3; yet, the main conclusions are unaffected. As ($|p| \rightarrow 0$) the FMO levels are shifted closer to the substrate Fermi level.

The results above clearly indicate that hybridization between the molecule and surface substantially impacts the charge injection energies. Still, hybridization alone does not clarify the role of surface plasmons. We will thus further disentangle the self-energy and inspect the contribution stemming *purely* from the charge density fluctuations in the substrate. We employ the self-energy decomposition scheme[59] and compute Σ of the molecular and substrate subspaces using the localized molecular orbitals basis (obtained by the orbital reconstruction[52]). In this localized molecular basis, the hybridization of molecular states has been artificially "suppressed".

The results support the picture of a large QP energy variation; there is more than a 1 eV difference between the facet center $(111)_{f1}$ and the facet edge $(111)_{f3}$ cases. (Figure 3) As in the hybridized basis result, the HOMO QP energy is closest to the Fermi level when the molecule sits at the (111) facet center. In contrast, the hybridized and "hybridization-suppressed" results differ for the LUMO, whose energy shifts toward the Fermi level as the molecule approaches the NP edge. In the absence of molecule−substrate orbital hybridization (the latter case), the propensity for direct injection thus trends together with the typical strength of local electric field enhancement when approaching to the nanostructure edge that has been studied before.[5,11] This observation is further illustrated in Figure 3c, showing that the electron injection barrier decreases by nearly 1.3 eV from the (111) facet center $(111)_{f1}$ to the edge $(111)_{f3}$. This plasmonic effect is captured by the variation in the correlation self-energy term, which contributes 66% to the QP energy difference between (111) facet center and the edge, further motivating our use of MBPT techniques. In practice, however, this trend is significantly altered by hybridization.

As a final note, we remark that the semilocal DFT orbitals have limited physical significance and suffer from over-delocalization,[60−63] yet, they provide physical insight into the role of hybridization on the QP energies. A deeper analysis of this effect will require the calculation of Dyson orbitals, which requires diagonalization of the full QP Hamiltonian matrix.[42,64,65] Such a step requires new developments in order to be computationally affordable for systems of the sizes discussed in this work.

In summary, we conducted a first-principles study of charge injection into molecules on a plasmonic gold surface using the many-body perturbation theory. The molecular quasiparticle energies take into account substrate-induced renormalization via coupling to charge density fluctuations (plasmons). The injection barrier varies substantially depending on the precise position on the nanoparticle surface; such variation is not seen in the mean-field (DFT) calculations and clearly illustrates the need for the inclusion of more elaborate (nonlocal and dynamical) correlation energies. The variation is on the order of hundreds of meV, and it significantly impacts the molecule's propensity to accept hot holes or electrons. We identify the

https://doi.org/10.1021/acs.jpclett.3c02223
J. Phys. Chem. Lett. 2023, 14, 8470−8476

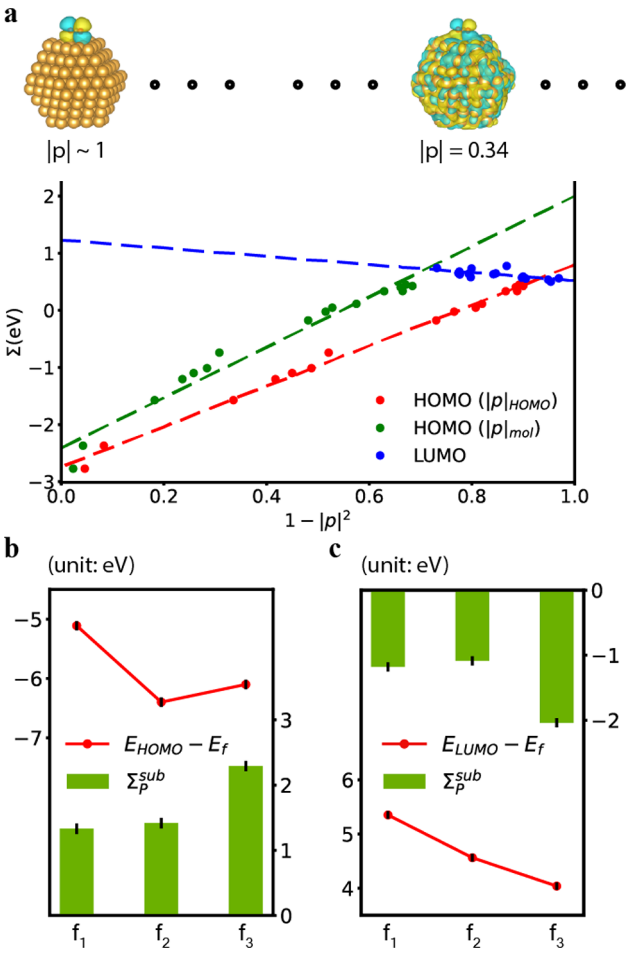

Figure 3. (a) The self-energy plot against the degree of hybridization $1 - |p|^2$. Dash lines show the fitting curves in the simplified relation: $\Sigma=|p|^2\Sigma_{mol}+(1-|p|^2)\Sigma_{sub}$. Noting that the slopes $k = \Sigma_{sub} - \Sigma_{mol}$ shown by the HOMO fitting on $|p|^2 = |p_{mol}|^2$ and $|p|^2 = |p_{HOMO}|^2$ change much, but they exhibit the same dependence on the hybridization with the surface. On the top, the hybridization suppressed HOMO and the hybridized HOMO in $(111)_{f1}$ are exemplified for the reconstructed orbital and KS canonical orbital that we used in this study. (b) and (c) summarize the results for E_{QP} and Σ_P^{sub} for hybridization suppressed orbitals on the NP $(111)_f$ sites. QP energy axis is the left, and the axis for Σ_P^{sub}, the polarization contribution term from the substrate, is the right. The stochastic errors in Σ_P^{sub} are shown by the black lines that are smaller than the red circle size.

degree of hybridization as one of the decisive effects on identifying the "hot spots" in terms of the vertical excitation in addition to the plasmon coupling factor. In fact, for the lowest electron injection energy, the hybridization overshadows the effect of the coupling purely on the surface charge fluctuations. It implies that in the structural design seeking the efficiency enhancement of plasmonically driven reactions should tune the chemical properties of the substrate to drive a higher degree of hybridization. While the pure substrate-driven renormalization (in the absence of hybridization) is strongest at the nanoparticle edges, the molecular states more readily delocalize over the NP substrate near the facet centers and completely alter the energy landscape. The direct injection mechanism needs to overcome a relatively large energy barrier, requiring strong nonequilibrium hole/particle distributions well below/above the Fermi levels. Even then, the energy variation for hot holes is significantly larger than that for the injection of hot electrons. In practice, the charge injection may be spatially limited to only very narrow regions of the nanoparticle facets (e.g., near the center of the 111 surfaces). This work underlines the need for the inclusion of nonlocal and dynamical correlation effects and motivates further research bringing condensed matter theoretical methods into the study of chemically relevant molecular excitations on (optically active) surfaces.

■ ASSOCIATED CONTENT

Supporting Information

The Supporting Information is available free of charge at https://pubs.acs.org/doi/10.1021/acs.jpclett.3c02223.

CO_2 geometry optimization on Au; preparation of Au substrates; hybridized single-particle state calculations; two-state fitting of self-energy on the Au_{260} NP; decomposition of self-energy calculations (PDF)

■ AUTHOR INFORMATION

Corresponding Author

Vojtech Vlcek − *Department of Chemistry and Biochemistry, University of California Santa Barbara, Santa Barbara, California 93106, United States; Department of Materials, University of California Santa Barbara, Santa Barbara, California 93106, United States;* orcid.org/0000-0002-2836-7619; Email: vlcek@ucsb.edu

Authors

Xiaohe Lei − *Department of Chemistry and Biochemistry, University of California Santa Barbara, Santa Barbara, California 93106, United States*

Annabelle Canestraight − *Department of Chemical Engineering, University of California Santa Barbara, Santa Barbara, California 93106, United States*

Complete contact information is available at: https://pubs.acs.org/10.1021/acs.jpclett.3c02223

Notes

The authors declare no competing financial interest.

■ ACKNOWLEDGMENTS

The authors thank Dr. Mariya Romanova and Dr. Guorong (Gwen) Weng for their technical support. This work was supported by the NSF CAREER award through grant No. DMR-1945098. Use was made of computational facilities purchased with funds from the National Science Foundation (CNS-1725797) and administered by the Center for Scientific Computing (CSC). The CSC is supported by the California NanoSystems Institute and the Materials Research Science and Engineering Center (MRSEC; NSF DMR 2308708) at UC Santa Barbara.

■ REFERENCES

(1) Moskovits, M. Surface roughness and the enhanced intensity of Raman scattering by molecules adsorbed on metals. *J. Chem. Phys.* **1978**, *69*, 4159−4161.

(2) Buntin, S. A.; Richter, L. J.; Cavanagh, R. R.; King, D. S. Optically driven surface reactions: Evidence for the role of hot electrons. *Physical review letters* **1988**, *61*, 1321.

(3) Zhu, X.-Y. Electron transfer at molecule-metal interfaces: A two-photon photoemission study. *Annu. Rev. Phys. Chem.* **2002**, *53*, 221−247.

(4) Christopher, P.; Xin, H.; Linic, S. Visible-light-enhanced catalytic oxidation reactions on plasmonic silver nanostructures. *Nature Chem.* **2011**, *3*, 467−472.
(5) Christopher, P.; Xin, H.; Marimuthu, A.; Linic, S. Singular characteristics and unique chemical bond activation mechanisms of photocatalytic reactions on plasmonic nanostructures. *Nature materials* **2012**, *11*, 1044−1050.
(6) Mukherjee, S.; Libisch, F.; Large, N.; Neumann, O.; Brown, L. V.; Cheng, J.; Lassiter, J. B.; Carter, E. A.; Nordlander, P.; Halas, N. J. Hot electrons do the impossible: plasmon-induced dissociation of H2 on Au. *Nano Lett.* **2013**, *13*, 240−247.
(7) Avanesian, T.; Christopher, P. Adsorbate specificity in hot electron driven photochemistry on catalytic metal surfaces. *J. Phys. Chem. C* **2014**, *118*, 28017−28031.
(8) Christopher, P.; Moskovits, M. Hot charge carrier transmission from plasmonic nanostructures. *Annu. Rev. Phys. Chem.* **2017**, *68*, 379−398.
(9) DuChene, J. S.; Tagliabue, G.; Welch, A. J.; Cheng, W.-H.; Atwater, H. A. Hot hole collection and photoelectrochemical CO2 reduction with plasmonic Au/p-GaN photocathodes. *Nano Lett.* **2018**, *18*, 2545−2550.
(10) Kim, Y.; Creel, E. B.; Corson, E. R.; McCloskey, B. D.; Urban, J. J.; Kostecki, R. Surface-Plasmon-Assisted Photoelectrochemical Reduction of CO2 and NO3- on Nanostructured Silver Electrodes. *Adv. Energy Mater.* **2018**, *8*, 1800363.
(11) Seemala, B.; Therrien, A. J.; Lou, M.; Li, K.; Finzel, J. P.; Qi, J.; Nordlander, P.; Christopher, P. Plasmon-mediated catalytic O2 dissociation on Ag nanostructures: hot electrons or near fields? *ACS Energy Letters* **2019**, *4*, 1803−1809.
(12) Abouelela, M. M.; Kawamura, G.; Matsuda, A. A review on plasmonic nanoparticle-semiconductor photocatalysts for water splitting. *Journal of Cleaner Production* **2021**, *294*, 126200.
(13) Martirez, J. M. P.; Bao, J. L.; Carter, E. A. First-principles insights into plasmon-induced catalysis. *Annu. Rev. Phys. Chem.* **2021**, *72*, 99−119.
(14) Jiang, X.; Huang, J.; Bi, Z.; Ni, W.; Gurzadyan, G.; Zhu, Y.; Zhang, Z. Plasmonic Active "Hot Spots"-Confined Photocatalytic CO2 Reduction with High Selectivity for CH4 Production. *Adv. Mater.* **2022**, *34*, 2109330.
(15) Lou, M.; Bao, J. L.; Zhou, L.; Naidu, G. N.; Robatjazi, H.; Bayles, A. I.; Everitt, H. O.; Nordlander, P.; Carter, E. A.; Halas, N. J. Direct H2S decomposition by plasmonic photocatalysis: Efficient remediation plus sustainable hydrogen production. *ACS Energy Letters* **2022**, *7*, 3666−3674.
(16) Wang, F.; Lu, Z.; Guo, H.; Zhang, G.; Li, Y.; Hu, Y.; Jiang, W.; Liu, G. Plasmonic Photocatalysis for CO2 Reduction: Advances, Understanding and Possibilities. *Chemistry−A European Journal* **2023**, *29*, e202202716.
(17) Hernandez, S.; Xia, Y.; Vlček, V.; Boutelle, R.; Baer, R.; Rabani, E.; Neuhauser, D. First-principles spectra of Au nanoparticles: from quantum to classical absorption. *Mol. Phys.* **2018**, *116*, 2506−2511.
(18) Wu, K.; Chen, J.; Mcbride, J. R.; Lian, T. Efficient hot-electron transfer by a plasmon-induced interfacial charge-transfer transition. *Science* **2015**, *349*, 632−635.
(19) Kale, M. J.; Christopher, P. Plasmons at the interface. *Science* **2015**, *349*, 587−588.
(20) Kelly, K. L.; Coronado, E.; Zhao, L. L.; Schatz, G. C. The optical properties of metal nanoparticles: the influence of size, shape, and dielectric environment. *J. Phys. Chem. B* **2003**, *107*, 668.
(21) Chernyshova, I. V.; Somasundaran, P.; Ponnurangam, S. On the origin of the elusive first intermediate of CO2 electroreduction. *Proc. Natl. Acad. Sci. U. S. A.* **2018**, *115*, E9261−E9270.
(22) Wu, Z.-Z.; Zhang, X.-L.; Niu, Z.-Z.; Gao, F.-Y.; Yang, P.-P.; Chi, L.-P.; Shi, L.; Wei, W.-S.; Liu, R.; Chen, Z.; et al. Identification of Cu (100)/Cu (111) interfaces as superior active sites for CO dimerization during CO2 electroreduction. *J. Am. Chem. Soc.* **2022**, *144*, 259−269.
(23) Egger, D. A.; Liu, Z.-F.; Neaton, J. B.; Kronik, L. Reliable energy level alignment at physisorbed molecule−metal interfaces from density functional theory. *Nano Lett.* **2015**, *15*, 2448−2455.
(24) Biller, A.; Tamblyn, I.; Neaton, J. B.; Kronik, L. Electronic level alignment at a metal-molecule interface from a short-range hybrid functional. *J. Chem. Phys.* **2011**, *135*, 164706.
(25) Liu, Z.-F.; Egger, D. A.; Refaely-Abramson, S.; Kronik, L.; Neaton, J. B. Energy level alignment at molecule-metal interfaces from an optimally tuned range-separated hybrid functional. *J. Chem. Phys.* **2017**, *146*, 092326.
(26) Bhandari, S.; Yamada, A.; Hoskins, A.; Payne, J.; Aksu, H.; Dunietz, B. D. Achieving Predictive Description of Negative Differential Resistance in Molecular Junctions Using a Range-Separated Hybrid Functional. *Advanced Theory and Simulations* **2021**, *4*, 2000016.
(27) VandeVondele, J.; Borštnik, U.; Hutter, J. Linear Scaling Self-Consistent Field Calculations with Millions of Atoms in the Condensed Phase. *J. Chem. Theory Comput.* **2012**, *8*, 3565−3573.
(28) Martin, R. M.; Reining, L.; Ceperley, D. M. *Interacting electrons*; Cambridge University Press, 2016.
(29) Rabilloud, F. Description of plasmon-like band in silver clusters: The importance of the long-range Hartree-Fock exchange in time-dependent density-functional theory simulations. *J. Chem. Phys.* **2014**, *141*, 144302.
(30) Baer, R.; Livshits, E.; Salzner, U. Tuned range-separated hybrids in density functional theory. *Annu. Rev. Phys. Chem.* **2010**, *61*, 85−109.
(31) Foster, M. E.; Wong, B. M. Nonempirically tuned range-separated DFT accurately predicts both fundamental and excitation gaps in DNA and RNA nucleobases. *J. Chem. Theory Comput.* **2012**, *8*, 2682−2687.
(32) Yang, Z.-h.; Sottile, F.; Ullrich, C. A. Simple screened exact-exchange approach for excitonic properties in solids. *Phys. Rev. B* **2015**, *92*, 035202.
(33) Skone, J. H.; Govoni, M.; Galli, G. Self-consistent hybrid functional for condensed systems. *Phys. Rev. B* **2014**, *89*, 195112.
(34) Zhan, J.; Govoni, M.; Galli, G. Nonempirical Range-Separated Hybrid Functional with Spatially Dependent Screened Exchange. *J. Chem. Theory Comput.* **2023**, *19*, 5851.
(35) Brawand, N. P.; Govoni, M.; Voros, M.; Galli, G. Performance and self-consistency of the generalized dielectric dependent hybrid functional. *J. Chem. Theory Comput.* **2017**, *13*, 3318−3325.
(36) Mejuto-Zaera, C.; Weng, G.; Romanova, M.; Cotton, S. J.; Whaley, K. B.; Tubman, N. M.; Vlček, V. Are multi-quasiparticle interactions important in molecular ionization? *J. Chem. Phys.* **2021**, *154*, 121101.
(37) Mejuto-Zaera, C.; Vlček, V. Self-consistency in G W Γ formalism leading to quasiparticle-quasiparticle couplings. *Phys. Rev. B* **2022**, *106*, 165129.
(38) Hedin, L. New method for calculating the one-particle Green's function with application to the electron-gas problem. *Phys. Rev.* **1965**, *139*, A796.
(39) Vlček, V.; Rabani, E.; Neuhauser, D. Quasiparticle spectra from molecules to bulk. *Physical Review Materials* **2018**, *2*, 030801.
(40) Vlček, V.; Rabani, E.; Neuhauser, D.; Baer, R. Stochastic GW Calculations for Molecules. *J. Chem. Theory Comput.* **2017**, *13*, 4997−5003.
(41) Li, J.; Jin, Y.; Rinke, P.; Yang, W.; Golze, D. Benchmark of GW Methods for Core-Level Binding Energies. *J. Chem. Theory Comput.* **2022**, *18*, 7570−7585.
(42) Kaplan, F.; Weigend, F.; Evers, F.; van Setten, M. J. Off-Diagonal Self-Energy Terms and Partially Self-Consistency in GW Calculations for Single Molecules: Efficient Implementation and Quantitative Effects on Ionization Potentials. *J. Chem. Theory Comput.* **2015**, *11*, 5152−5160.
(43) Rignanese, G.-M.; Blase, X.; Louie, S. Quasiparticle Effects on Tunneling Currents: A Study of C 2 H 4 Adsorbed on the Si (001)-(2× 1) Surface. *Physical review letters* **2001**, *86*, 2110.

https://doi.org/10.1021/acs.jpclett.3c02223
J. Phys. Chem. Lett. 2023, 14, 8470−8476

(44) Tamblyn, I.; Darancet, P.; Quek, S. Y.; Bonev, S. A.; Neaton, J. B. Electronic energy level alignment at metal-molecule interfaces with a G W approach. *Phys. Rev. B* **2011**, *84*, 201402.
(45) Pham, T. A.; Nguyen, H.-V.; Rocca, D.; Galli, G. G. W calculations using the spectral decomposition of the dielectric matrix: Verification, validation, and comparison of methods. *Phys. Rev. B* **2013**, *87*, 155148.
(46) Neuhauser, D.; Gao, Y.; Arntsen, C.; Karshenas, C.; Rabani, E.; Baer, R. Breaking the Theoretical Scaling Limit for Predicting Quasiparticle Energies: The Stochastic G W Approach. *Physical review letters* **2014**, *113*, 076402.
(47) Vlček, V.; Li, W.; Baer, R.; Rabani, E.; Neuhauser, D. Swift *GW* beyond 10,000 electrons using sparse stochastic compression. *Phys. Rev. B* **2018**, *98*, 075107.
(48) Hori, Y. Electrochemical CO2 reduction on metal electrodes. *Modern aspects of electrochemistry* **2008**, *42*, 89−189.
(49) Giannozzi, P.; Baroni, S.; Bonini, N.; Calandra, M.; Car, R.; Cavazzoni, C.; Ceresoli, D.; Chiarotti, G. L.; Cococcioni, M.; Dabo, I.; et al. QUANTUM ESPRESSO: a modular and open-source software project for quantum simulations of materials. *J. Phys.: Condens. Matter* **2009**, *21*, 395502.
(50) Weng, G.; Romanova, M.; Apelian, A.; Song, H.; Vlcek, V. Reduced scaling of optimal regional orbital localization via sequential exhaustion of the single-particle space. *J. Chem. Theory Comput.* **2022**, *18*, 4960−4972.
(51) Weng, G.; Pang, A.; Vlček, V. Spatial Decay and Limits of Quantum Solute−Solvent Interactions. *J. Phys. Chem. Lett.* **2023**, *14*, 2473−2480.
(52) Weng, G.; Vlček, V. Efficient treatment of molecular excitations in the liquid phase environment via stochastic many-body theory. *J. Chem. Phys.* **2021**, *155*, 054104.
(53) Atkinson, S.; Brundle, C.; Roberts, M. Ultra-violet and X-ray photoelectron spectroscopy (UPS and XPS) of CO, CO 2, O 2 and H 2 O on molybdenum and gold films. *Faraday Discuss. Chem. Soc.* **1974**, *58*, 62−79.
(54) Onida, G.; Reining, L.; Rubio, A. Electronic excitations: density-functional versus many-body Green's-function approaches. *Reviews of modern physics* **2002**, *74*, 601.
(55) Blase, X.; Attaccalite, C.; Olevano, V. First-principles GW calculations for fullerenes, porphyrins, phtalocyanine, and other molecules of interest for organic photovoltaic applications. *Phys. Rev. B* **2011**, *83*, 115103.
(56) Rostgaard, C.; Jacobsen, K. W.; Thygesen, K. S. Fully self-consistent GW calculations for molecules. *Phys. Rev. B* **2010**, *81*, 085103.
(57) Kümmel, S.; Kronik, L. Orbital-dependent density functionals: Theory and applications. *Rev. Mod. Phys.* **2008**, *80*, 3.
(58) Neaton, J. B.; Hybertsen, M. S.; Louie, S. G. Renormalization of molecular electronic levels at metal-molecule interfaces. *Physical review letters* **2006**, *97*, 216405.
(59) Romanova, M.; Vlček, V. Decomposition and embedding in the stochastic GW self-energy. *J. Chem. Phys.* **2020**, *153*, 134103.
(60) Mori-Sánchez, P.; Cohen, A. J.; Yang, W. Localization and delocalization errors in density functional theory and implications for band-gap prediction. *Physical review letters* **2008**, *100*, 146401.
(61) Cohen, A. J.; Mori-Sánchez, P.; Yang, W. Insights into current limitations of density functional theory. *Science* **2008**, *321*, 792−794.
(62) Kim, M.-C.; Sim, E.; Burke, K. Understanding and reducing errors in density functional calculations. *Physical review letters* **2013**, *111*, 073003.
(63) Johnson, E. R.; Otero-De-La-Roza, A.; Dale, S. G. Extreme density-driven delocalization error for a model solvated-electron system. *J. Chem. Phys.* **2013**, *139*, 184116.
(64) Caruso, F.; Rinke, P.; Ren, X.; Rubio, A.; Scheffler, M. Self-consistent G W: All-electron implementation with localized basis functions. *Phys. Rev. B* **2013**, *88*, 075105.
(65) Rusakov, A. A.; Zgid, D. Self-consistent second-order Green's function perturbation theory for periodic systems. *J. Chem. Phys.* **2016**, *144*, 054106.

https://doi.org/10.1021/acs.jpclett.3c02223
J. Phys. Chem. Lett. 2023, 14, 8470−8476